Low Work Function Ytterbium Silicide Contact for Doping-Free Silicon Solar Cells

Cho, Jinyoun; Radhakrishnan, Hariharsudan Sivaramakrishnan; Payo, Maria Recaman; Debucquoy, Maarten; VAN DER HEIDE, Arvid; GORDON, Ivan; Szlufcik, Jozef & POORTMANS, Jef (2020) Low Work Function Ytterbium Silicide Contact for Doping-Free Silicon Solar Cells. In: ACS APPLIED ENERGY MATERIALS, 3 (4) , p. 3826 -3834.

DOI: 10.1021/acsaem.0c00256
Handle: http://hdl.handle.net/1942/31374

Low work function Yb silicide contact for doping-free silicon solar cells

Jinyoun Cho[a,b*], Hariharsudan Sivaramakrishnan Radhakrishnan[b], Maria Recaman Payo[b], Maarten Debucquoy[b], Arvid van der Heide[b], Ivan Gordon[b], Jozef Szlufcik[b], and Jef Poortmans[a,b,c]

[a]ESAT department, KU Leuven, Kasteelpark Arenberg 10, Leuven 3001, Belgium

[b]imec (partner in EnergyVille), Kapeldreef 75, Leuven 3001, Belgium

[c]University Hasselt, Martelarenlaan 42, Hasselt 3500, Belgium

*Corresponding author: jinyoun.cho@eu.umicore.be

*Current address: Umicore, Watertorenstraat 33, B-2250 Olen, Belgium

Keywords: doping-free cells, Yb silicide, pinning, electron-selective contact, passivating contact

Abstract

Metal silicide is a well-known material for contact layers, however, it has not been tested in the context of doping-free carrier selective contacts. Thin film deposition of an appropriate metal with mild annealing treatment is an interesting alternative to the more complex depositions of other compound materials. Reaction of Yb deposited on top an i-a-Si:H passivation layer results in the formation of $YbSi_x$ on top of a remnant i-a-Si:H following a low-temperature anneal below 200 °C. Such a contact is an interesting candidate as a doping-free electron-selective contact. Detailed investigation of the i-a-Si/$YbSi_x$ contact shows that Yb thickness, i-a-Si:H thickness and silicidation annealing conditions play a significant role in determining the recombination current density ($J_{0,metal}$) and the contact resistivity (ρ_c). Low $J_{0,metal}$ of 5 fA/cm^2 and low ρ_c below 0.1 Ω.cm were independently demonstrated for such i-a-Si:H/$YbSi_x$ contacts. We also demonstrate that low-temperature silicidation can be combined with

contact sintering (160 °C/25 min) or module lamination (160 °C/20 min), which are potential pathways for process simplification. Combining the optimised i-a-Si:H/$YbSi_x$ electron contact with MoO_x based hole contact in the MolYSili doping-free cell (i-a-Si:H/MoO_x+ i-a-Si:H/$YbSi_x$), we achieved 16.7 % in average efficiency and 17.0 % for the champion cell. Furthermore, the $YbSi_x$ contact stability was evaluated at module level and excellent thermal stability of the MolYSili laminate was demonstrated using the damp-heat test method (humidity 85 %, 85 °C, 1000 h), where the laminated MolYSili cell did not show any degradation in the cell efficiency. This is the first proof-of-concept demonstration of a stable silicide-based contact for low-temperature processed doping-free solar cells.

1. Introduction

Historically, a p-n semiconductor junction has been used in crystalline silicon (c-Si) solar cells to separate photogenerated electron-hole pairs and collect minority charge-carriers before they recombine. In addition, a high-low junction (i.e. p/p^+ or n/n^+) has been used for the base contact to reduce contact resistivity (ρ_c), and to lower surface recombination using field-effect, hence the name back surface field (BSF) when used at the backside. Doped c-Si regions or doped thin film layers have been used to form such p-n as well as high-low homo- or hetero-junctions.

Typically, for silicon homo-junction solar cells, the doping process to form a doped region in c-Si is based on thermal diffusion of dopant atoms from a dopant source, such as borosilicate-glass (BSG) or phosphosilicate-glass (PSG) [1–3]. To avoid unwanted metal impurity contamination[4] during thermal diffusion and the subsequent process steps, pre- and post-cleaning processes are needed. For silicon heterojunction (SHJ) solar cells, n-type or p-type amorphous silicon (n,p-a-Si:H) is stacked on intrinsic a-Si:H (i-a-Si:H). However, such heavily-doped regions in c-Si or doped a-Si:H thin films result in unwanted power losses due to free-carrier absorption and increased Auger recombination [5,6]. Therefore, the PV research community has explored options to fabricate solar cells without doping processes or doped layers due to the potential for a simpler fabrication process flow and lower optoelectrical losses [7–15].

However, achieving a low recombination current density at the metalized area ($J_{0,metal}$) *and* a low ρ_c simultaneously is very challenging without a highly-doped c-Si region at the surface or a doped thin

film layer. As a consequence, many works in the field of doping-free solar cells have focused on attaining low $J_{0,metal}$ without compromising on ρ_c, with promising results. For the hole contact, high work function metal oxides, especially MoO_x, have been investigated intensively [16–22]. For the electron contact, low work function metal oxides [23–26], metal nitrides [27,28], rare-earth metal fluorides [29,30] and low work function metals [22,31–38] have been studied.

While fabricating solar cells using metal silicides with high and low work function has been suggested before [39,40], investigation of metal silicides in the context of doping-free carrier-selective contacts have not been prevalent, even though metal silicides, such as $NiSi_x$, $TiSi_x$, and $PtSi_x$, are well-known materials in semiconductor devices [41–46]. We propose that low work function and high work function metal silicides in combination with a passivating i-a-Si:H layer are attractive candidates to be applied as electron-and hole-selective contacts, respectively.

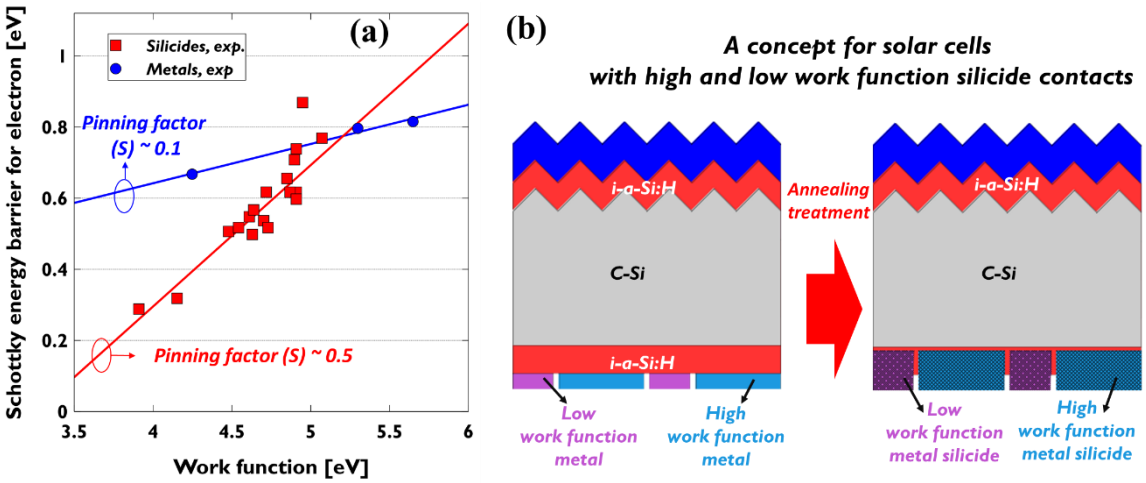

Figure 1. (a) Dependence of the metal- or metal silicides work function on the Schottky energy barrier height; reproduced with permission from the publisher [47]. (b) A concept of all-metal silicide back-contacted solar cell. Two-side contacted cell is also possible.

Figure 1 (a) clearly illustrates the benefit of using a metal silicide contact compared to a typical metal-semiconductor (MS) contact. When the Si surface is contacted by a metal or metal silicide, a Schottky energy barrier (Φ_B) is formed depending on the work function of contacting metal or metal silicide as well as the pinning factor, which determines the effectiveness of the work function of the contacting material in controlling the Φ_B. The pinning of the Fermi level of the metal or metal silicide ($E_{F,metal}$ or $E_{F,metal\ silicide}$) on c-Si surface can be quantitatively compared using the slope (S, pinning factor) in Figure 1 (a). The pinning factor for a metal contact on c-Si surface varies from 0.1 [47] to 0.3 [48,49], however, the pinning factor for a metal-silicide contact on the same surface is about 0.5. This means that the work

function of the metal-silicide influences the energy band bending at the contact region more strongly. Strong and favorable band bending is beneficial for achieving low ρ_c. Since amorphous silicon (a-Si:H) surfaces also exhibit similar metal Fermi level pinning behaviour[48], metal silicide on a-Si:H is an interesting contact structure to investigate for heterojunction solar cells because it combines the appropriately induced strong band bending at the c-Si surface due to the silicide and the high-quality passivation of the c-Si surface rendered by i-a-Si:H.

Typically, metal silicides are formed at relatively high temperatures above 400 °C [50], which is too high for a-Si:H based silicon heterojunction solar (SHJ) cells. Some silicides such as $NiSi_x$[51] and $TiSi_x$[42], however, can be formed at low temperatures below 200 °C. Also, silicide formation by reaction between i-a-Si:H and metal can be achieved with a low-temperature anneal below 200 °C. With this method of metal silicide formation, all-metal silicide-contacted solar cells with different architectures can be envisaged. As an example, interdigitated-back-contact (IBC) cells based on i-a-Si:H/metal silicide contact could be fabricated as shown in Figure 1 (b).

In this work, we use ytterbium silicide ($YbSi_x$) formed by reacting a-Si:H and Yb using a low temperature anneal below 200 °C as part of an electron-selective contact for two-side contacted silicon heterojunction (SHJ) solar cells. $YbSi_x$ has been widely studied in the microelectronics industry for its application in semiconductor devices such as MOSFETs and FinFETs [43,45,46,52,53]. Optimization of the novel $YbSi_x$ contact was performed to minimize ρ_c and $J_{0,metal}$. The optimized $YbSi_x$ electron contact was then integrated with MoO_x-based hole contact to produce fully doping-free solar cells, which we call as MolYSili (Molybdenum oxide with Ytterbium Silicide) solar cells. In order to demonstrate the thermal stability of the MolYSili cells at module level, a one-cell laminate was fabricated to study its performance under damp-heat testing conditions (humidity 85 %, 85 °C, 1000 h).

2. Experimental methods

2.1. Test structures for $J_{0,passi}$, $J_{0,metal}$ and ρ_c evaluation

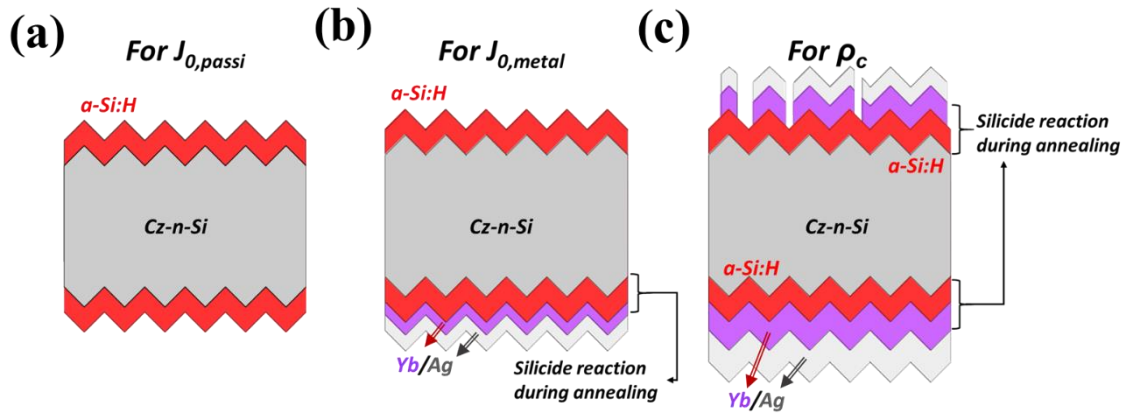

Figure 2. Schematic sample structures for (a) $J_{0,passi}$, (b) $J_{0,metal}$ and (c) ρ_c extraction.

Double-side textured (3 Ω·cm, 180 µm thickness after texturing process) n-type Czochralski (Cz) Si wafers were used to prepare test samples to measure $J_{0,passi}$, $J_{0,metal}$ and ρ_c to assess the performance of the $YbSi_x$-based passivating contact under development. After wafer cleaning using O_3/HCl/deionized H_2O and HF/HCl solutions, an 8 nm thick intrinsic a-Si:H layer was deposited on the front and rear sides of the substrates by plasma-enhanced chemical vapor deposition (PECVD). At this stage, lifetime measurements were performed on samples with a structure as shown in Figure 2 (a), using quasi-steady-state photo-conductance (QSSPC) and the $J_{0,total}$ for this structure was determined. From this, the $J_{0,passi}$ values were calculated based on Eq. (1)

$$J_{0,total} = 2 \times J_{0,passi} + J_{0,bulk} \qquad \text{Equation (1)}$$

The $J_{0,bulk}$ of the Cz wafer was determined to be approximately 3 fA/cm^2, by comparing the $J_{0,total}$ of a Cz wafer with that of a high-quality float zone wafer (n-type, 200 µm, 3.3 Ω·cm), both symmetrically passivated using the same i-a-Si:H layers. The $J_{0,total}$ was calculated from implied-V_{OC} (iV_{OC}) assuming a typical J_{SC} value of 36 mA/cm^2 in our SHJ cells.

For determination of $J_{0,metal}$ with different Yb thickness, Yb/Ag of 5 nm/5 nm or 7.5 nm / 3 nm was sequentially thermally evaporated on top of the i-a-Si:H at the rear side without breaking the vacuum. Silicidation was achieved using rapid thermal annealing (RTA) at 150 °C for 10 min. Again, QSSPC measurements were performed on a structure as shown in Figure 2 (b). From this, $J_{0,metal}$ can be calculated based on Eq. (2)

$$J_{0,metal} = J_{0,total} - \left(J_{0,front} + J_{0,bulk}\right), \quad \text{where } J_{0,front} = J_{0,passi} \qquad \text{Equation (2)}$$

The $J_{0,front}$ of samples with the structure as shown in Figure 2 (b) was assumed to have the same value as $J_{0,passi}$ of samples without metal (Figure 2 (a)). For accurate evaluation of $J_{0,a\text{-}Si:H/YbSix}$, $J_{0,passi}$ was extracted again on samples which underwent the same silicidation annealing conditions.

For ρ_c characterization, circular Yb/Ag front metal contacts were deposited using a metal shadow mask, with varying diameters (250-2000 µm), while a full area contact was formed on the rear side of the ρ_c samples. Firstly, a fixed Yb thickness of 30 nm was used for studying the impact of silicidation annealing on ρ_c at two different temperatures of 150 °C and 180 °C for up to 30 min. Secondly, to understand the influence of Yb thickness on ρ_c, the Yb thicknesses were varied i.e. 2.5, 5.0, 7.5 and 30 nm and sequential silicidation annealing treatments at 150 °C and 175 °C for 10 min each were done.

All ρ_c values for the electron contact were determined using the two-contact-two-terminal method in order to include all resistive components of the contact in the measured ρ_c [34,54]. More details on the methods used to determine ρ_c and J_0 can be found elsewhere [34,37,38].

The thin film layers making up the silicide-based contact and their interfaces, as well as the elemental distribution, were analyzed by transmission electron microscopy (TEM), high-angle annular dark-field imaging in scanning TEM (HAADF-STEM) and energy-dispersive X-ray spectroscopy (EDX).

2.2. Solar cells

Three types of solar cells were fabricated in this work. The cell fabrication process flows are summarized in Figure 3 (a), with the corresponding schematic structures of the 3 cell types depicted in Figure 3 (b)-(d). All 3 cell structures investigated had the same hole-selective contact featuring the i-a-Si:H/MoO_x/ITO/Ag stack on the front side [21,22]. On the rear side, different electron-selective contacts were applied: i-a-Si:H/Yb/Ag and i-a-Si:H/$YbSi_x$/Ag as doping-free electron-selective contact candidates, and i/n-a-Si:H/ITO/Ag as the classical SHJ reference. These contact structures will simply be referred to as Yb-contacted, MolYSili (i-a-Si:H/MoO_x hole contact + i-a-Si:H/$YbSi_x$ electron contact) and classical SHJ electron contact cells, respectively. Note that the thickness of $YbSi_x$ and remaining a-Si:H may differ depending on the initial Yb thickness and silicidation annealing conditions used after Yb deposition.

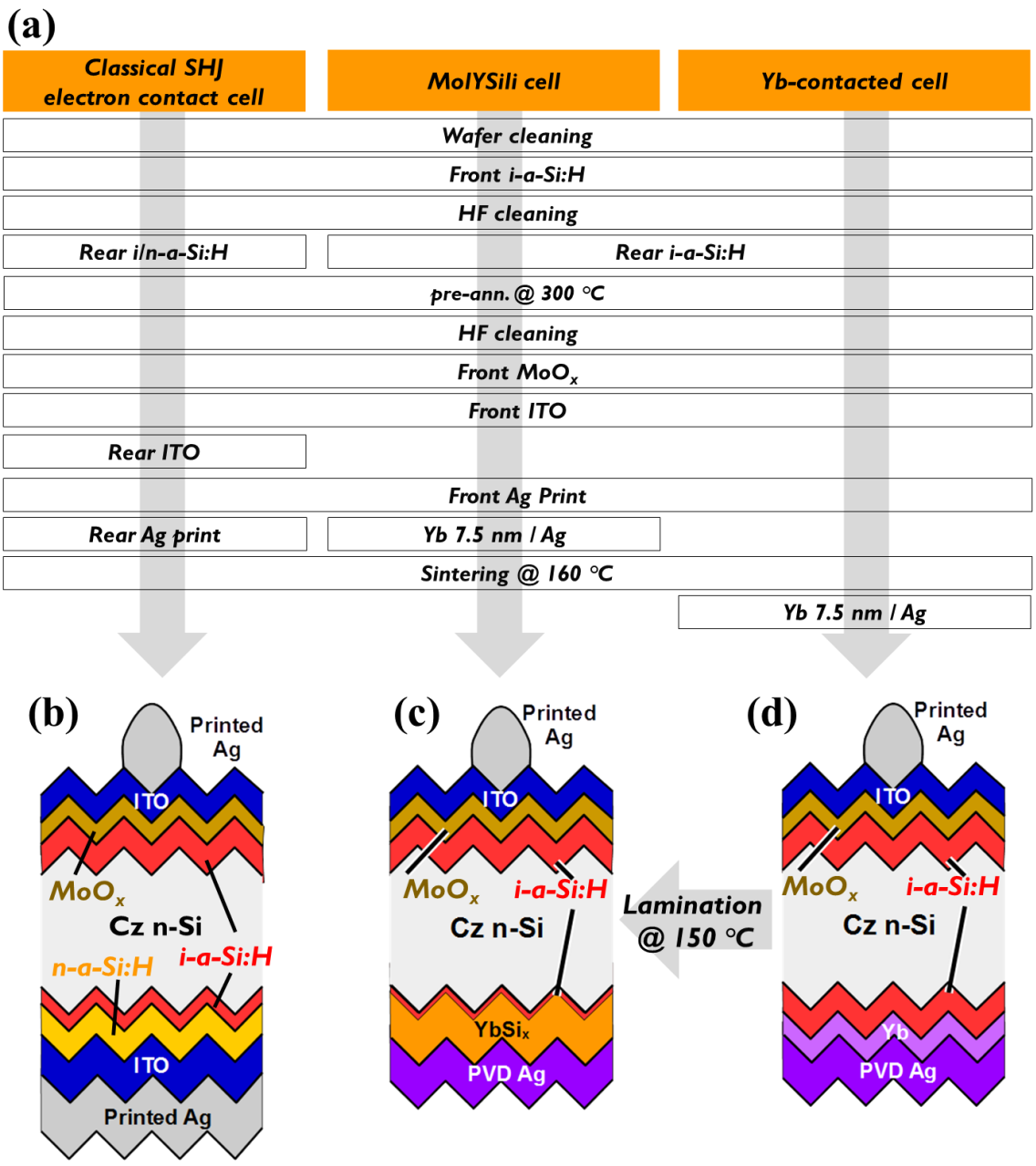

Figure 3. Cell fabrication process flows (a) and cross-sectional schematics ((b), (c) and (d)) for 3 different solar cells with the same MoO_x hole contact at the front and different electron contacts, namely, classical SHJ electron contact-, $YbSi_x$-(MolYSili) and Yb contacts at the rear, respectively. Pre-ann = pre-annealing before MoO_x deposition.

N-type Cz-Si wafers (3 Ω·cm, 180 µm thickness after texturing process) with double-side textured surfaces were used. After HF:HCl:O_3 and HF:HCl cleaning [55], an 8 nm thick i-a-Si:H layer was deposited on the front side using PECVD. Subsequently, after a short HF cleaning, i-a-Si:H of 8 nm was deposited on the rear for the two doping-free contact groups, and a stack of 4 nm thick i-a-Si:H and 8 nm thick n-a-Si:H was deposited for the classical SHJ reference group.

All cells were annealed at 300 °C for 20 min in N_2. After a HF cleaning, a MoO_x layer of 6 nm was evaporated on the front side of all cell groups. Subsequently, an ITO layer with a thickness of 70 nm

was deposited by sputtering on the front-side of all cells, and with a thickness of 110 nm on the rear-side only for the classical SHJ electron contact cells. Similarly, a Ag front grid (with fingers 80 μm wide, 17 μm high) was screen-printed for all cell groups, while screen-printed Ag on the rear-side was only applied for the classical SHJ electron contact cells (Figure 3 (b)).

For the Yb contacted cells and MolYSili cells, a stack of 7.5 nm thick Yb and 150 nm thick Ag was thermally evaporated without vacuum break on the rear-side. For the MolYSili cells (Figure 3 (c)), sintering was done after Yb/Ag deposition, which simultaneously results in the formation of $YbSi_x$, while for the Yb-contacted cell group (Figure 3 (d)), the contact sintering process was applied before deposition of Yb/Ag. The sintering process was done using a belt furnace at 160 ˚C for about 25 min in N_2 atmosphere. For the Yb-contacted cells and MolYSili cells, Yb thickness of 7.5 nm was tested. As the final step, the wafers were diced into solar cells of 5 x 5 cm^2 with an active cell area of 4 x 4 cm^2.

The illuminated IV parameters were measured with an aperture opening of the same size as the active cell area of 4 × 4 cm^2 under calibrated illumination (AM 1.5G, 1000 W/m^2 at 25 °C). External quantum efficiency (EQE) and reflectance were measured using an illumination spot size of 1.5 × 1.5 cm^2. Therefore, the EQE and reflectance results include shading and reflection effects of the front metal grid.

2.3. One-cell mini-modules

For damp-heat testing, one-cell mini-modules (glass/glass) were fabricated using an Yb-contacted cell shown in Figure 3 (a) and (d) with a pre-annealing treatment at 300 °C and initial Yb thickness of 7.5 nm. An UV-blocking ethylene vinyl acetate (EVA) sheet, a smart-wire connection technology (SWCT) foil (from Meyer Burger) and glass were used for encapsulation. A solder-coated ribbon was used to connect the smart wires and bring the electrical contacts of the cell to outside the single cell laminate. A butyl rubber tape was applied for hermetic sealing at the edges. The lamination process was carried out at 150 °C for about 20 min. During the course of the damp heat test (85 °C/85% humidity/1000 h), illuminated IV curves (AM 1.5, 1000 W/m^2 at 25 °C) were measured after every 250 h. An aperture area of 4 × 4 cm^2 was used for these measurements by using an opaque black tape around the edge of the active cell area. The same module structure and test methods were reported in [21].

3. Results and discussion

3.1. Low-temperature silicidation by reaction of Yb with a-Si:H

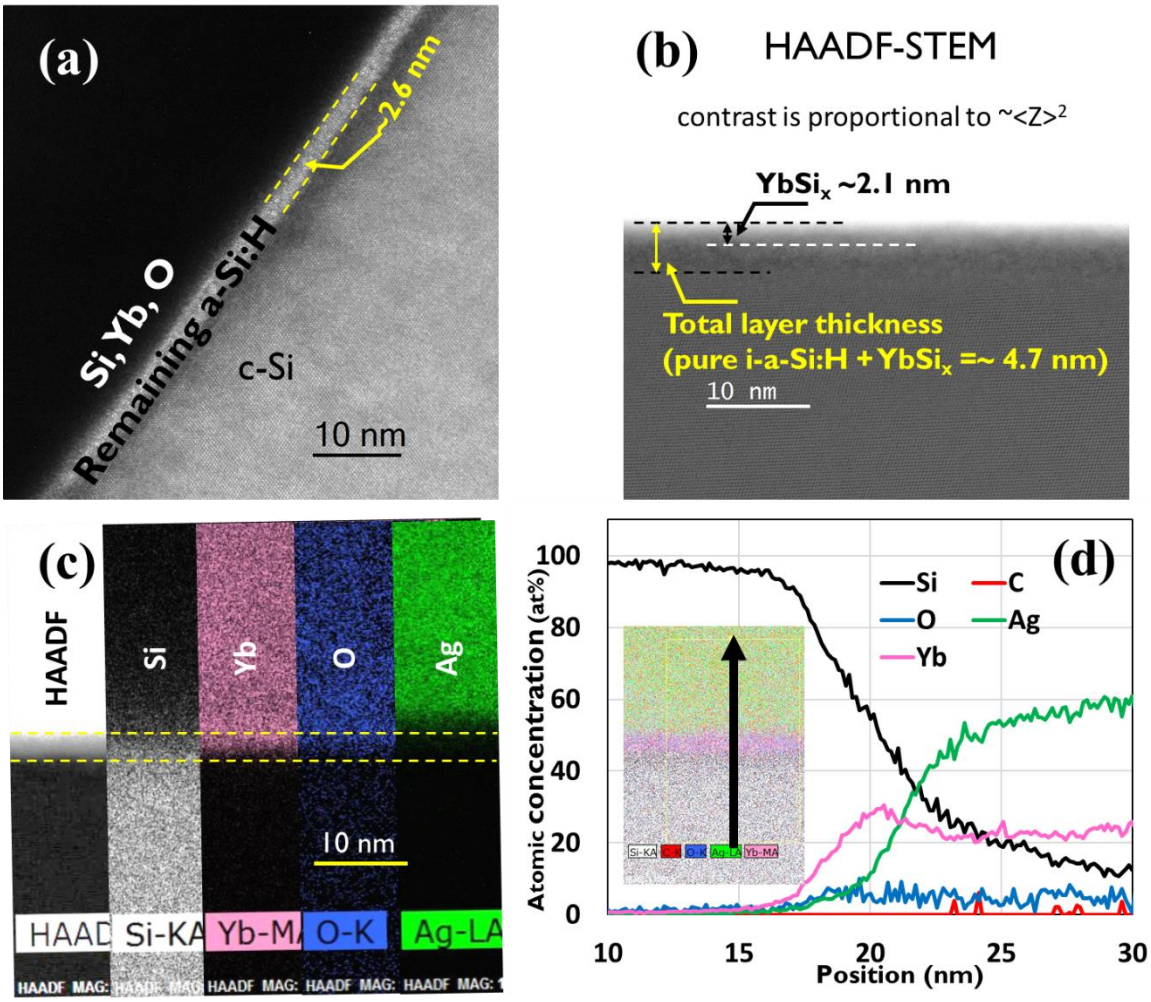

Figure 4 (a) TEM image for the annealed sample at 180 °C for 30 min. (b) high-angle annular dark-field imaging in scanning transmission electron microscopy (HAADF-STEM), (c) EDX map and (d) chemical profile for the chemical element distribution at the electron contact region.

The possible formation of $YbSi_x$ by reaction of Yb with i-a-Si:H at low temperatures below 200 °C was investigated by TEM, HAADF-STEM and EDX (Figure 4). HAADF-STEM contrast is proportional to $\sim Z^2$ where Z is the atomic number. Therefore, a different material composition of layers lead to a different contrast of the HAADF-STEM images. The interfaces of the contact layers of a sample after a silicidation anneal, with the largest thermal budget (180 °C for 30 min) used in this work, is shown in Figure 4. Note that for the sample shown in Figure 4, an additional HF clean was done to remove the native SiO_x that was grown due to the long storage time of more than a month. Thus, the final i-a-Si:H layer before silicidation anneal is expected to be around of 4-5 nm in thickness.

From the TEM image of Figure 4 (a), it can be seen that after the silicidation anneal at 180 °C for 30 min, the remaining pure a-Si:H layer thickness was only about 2.6 nm, indicating that some a-Si:H has

been consumed during this annealing process, suggesting the formation of $YbSi_x$ in between Yb metal and i-a-Si:H. This is supported by the higher resolution HAADF-STEM image of the same interface (Figure 4 (b)), which shows an amorphous layer of about 4.7 nm in thickness, consisting of two distinct layers, having a different Z contrast. The brighter layer closer to Yb metal is expected to a product of the silicidation anneal i.e. $YbSi_x$. Conclusive proof of silicidation is obtained through an EDX analysis of the interfaces. Figure 4 (c) shows the elemental distribution at the contact region. In the area demarcated by the yellow dashed lines, Si, Yb and O signals can be seen to overlap. We assume that the O signal could be due to surface oxidation due to the air exposure during TEM sample preparation. Therefore, we interpret this amorphous layer in-diffused with Yb as $YbSi_x$, with a thin unreacted a-Si layer between $YbSi_x$ and c-Si. Thus, approximately 2 nm of a-Si:H has reacted with Yb to form $YbSi_x$ after annealing at 180 °C for 30 min. Although the profile may be not sufficient to conclude the value of x in $YbSi_x$, it seems that x varies along with depth reaching a value of about 1.9, at the position with a peak in Yb concentration (see Figure 4 (d)). In addition, it is also observed that there is considerable alloying between Yb and Ag, which would compete with $YbSi_x$ formation.

Note that Yb diffusion into a-Si:H did not result in metal-induced crystallization (MIC) as observed for other metals such as Al, Au and Ni [56,57]. We believe that it is important to have some remaining unreacted and non-crystallised a-Si:H-layer on c-Si to maintain the passivation properties of the contact structure. In this particular case, the remnant i-a-Si:H after silicidation was only 2.6 nm thick, which is too thin to ensure good passivation, and above 4 nm would be needed.

3.2. Impact of silicidation on passivation

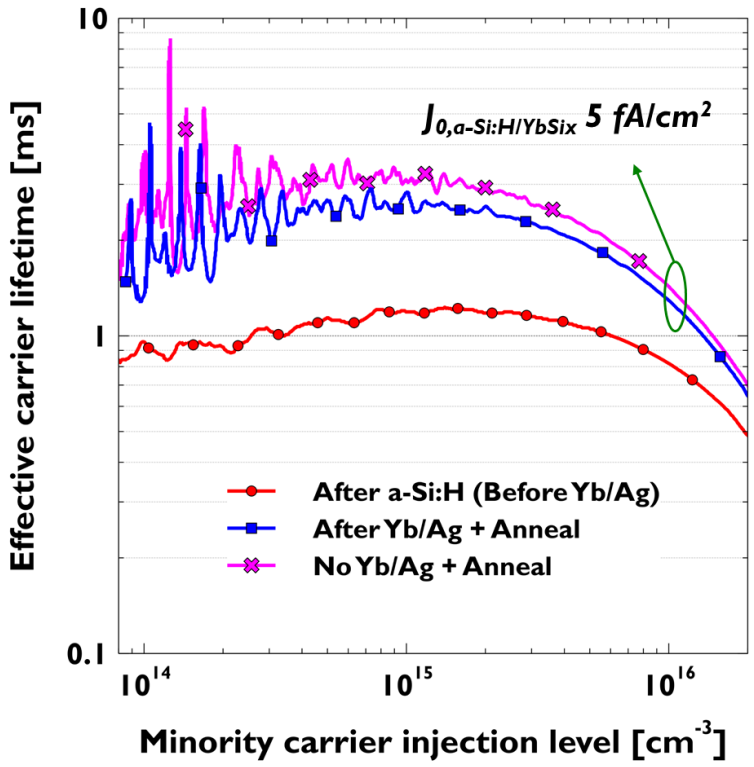

Figure 5. Injection-level dependent effective minority carrier lifetime and the extracted J0 value of samples with/without metal (5 nm Yb/5 nm Ag) stack and before/after the silicidation anneal at 150 °C for 10 min.

Achieving low $J_{0,metal}$ (below 30 fA/cm^2) and low ρ_c (below 0.1 Ω·cm^2) at the contacts are important for realizing high-efficiency solar cells[58,59]. In order to evaluate contact passivation, $J_{0,passi}$ and $J_{0,metal}$ (= $J_{0,a\text{-}Si:H/YbSix}$) were extracted from minority carrier lifetime measurements on samples with structures as shown in Figure 2 (a) and (b), before and after silicidation anneal at 150 °C for 10 min. As described in Section 2.1, the starting i-a-Si:H thickness for the samples of this study was around 8 nm while the Yb and Ag thickness was limited to enable photoconductance measurement. As plotted in Figure 5, after the silicidation anneal at 150 °C for 10 min, J_0 values are significantly decreased. For the contact with 5 nm thick Yb, significantly low $J_{0,a\text{-}Si:H/YbSix}$ of 5 fA/cm^2 was achieved, even though some i-a-Si:H would have been consumed by the silicidation process, as detailed in Section 3.1. Annealing a sample under the same conditions but without the metal stack also improved the lifetime and led to a similar value for $J_{0,passi}$ of 6 fA/cm^2. Chemical passivation by i-a-Si:H by means of hydrogenation of the c-Si/a-Si interface is the major passivation mechanism for the investigated sample structures. Since after annealing, both non-metallized and metalized samples achieved a similarly low J_0 value of 5-6 fA/cm^2, it can be expected that the observed improvement in passivation is due to enhanced hydrogenation of the c-Si/a-Si interface

due to the annealing, which helps to relocate some bulk H to the interface. However, given that the same level of passivation was achieved in the annealed sample despite the fact that some i-a-Si:H would have been consumed by the silicidation process, this could suggest possible contribution of field passivation from the $YbSi_x$ that is formed.

3.3. Investigation of factors influencing the ρ_c of $YbSi_x$-based contacts

The ρ_c of Yb-based contacts was evaluated using the test structure shown in Figure 2 (c). As a first step, the effect of post-annealing i.e. silicidation anneal on the ρ_c was studied at two different temperatures of 150 °C and 180 °C, while the annealing time was varied up to 30 min (see Figure 6). The thickness of Yb was 30 nm. The thickness of the i-a-Si:H prior to silicidation was around 4-5 nm.

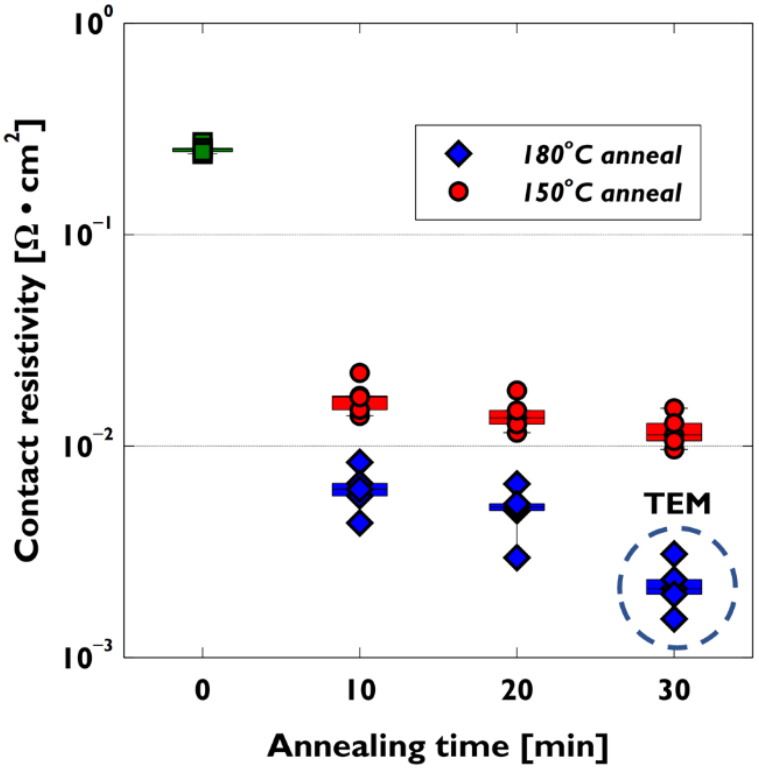

Figure 6. Contact resistivity of a-Si:H/$YbSi_x$ contact after annealing at 150 °C or 180 °C for different times. TEM shown in Figure 4 was measured using the post-annealed sample at 180 °C for 30 min.

As discussed in the introduction, metal Fermi level pinning occurs at the a-Si:H/metal interface, which leads to high $\rho_c > 0.1\ \Omega \cdot cm^2$, as also observed for the i-a-Si:H/Yb contact structure (see data points at 0 min annealing time in Figure 6). However, after the silicidation annealing treatment, a promising trend was found (see Figure 6). Unlike the usual increasing trend of ρ_c with annealing treatment observed in MIS contacts [37,60], the ρ_c of the i-a-Si:H/Yb contact was drastically reduced upon annealing for just 10 min at 150 °C by more than an order of magnitude compared to the initial value. During this anneal,

presumably silicidation at the a-Si:H/Yb interface occurs, resulting in the formation of $YbSi_x$. The ρ_c was reduced even further by annealing at a high temperature of 180 °C and for longer durations up to 30 min, which could lead to more silicidation, limited only by the entire consumption of either the Yb or the a-Si:H layers. The samples annealed with the highest thermal budget i.e. 180 °C for 30 min showed the lowest ρ_c. Given that the pinning factor, *S*, for silicides is higher than that for metals, the reduction in ρ_c is expected to be mainly due to the formation of $YbSi_x$.

The final metal silicide thickness is generally determined by the metal thickness when supply of Si is abundant and the total thermal budget (silicidation anneal, lamination, etc.) is long enough[50]. Therefore, the right Yb thickness should be chosen such that Yb is the limiting material in the formation of $YbSi_x$ in order to avoid complete consumption of i-a-Si:H and for better thermal stability of the contact such that the contact structure and characteristics do not change with time during operation. To this end, ρ_c was investigated as a function of Yb thickness with silicidation annealing treatments.

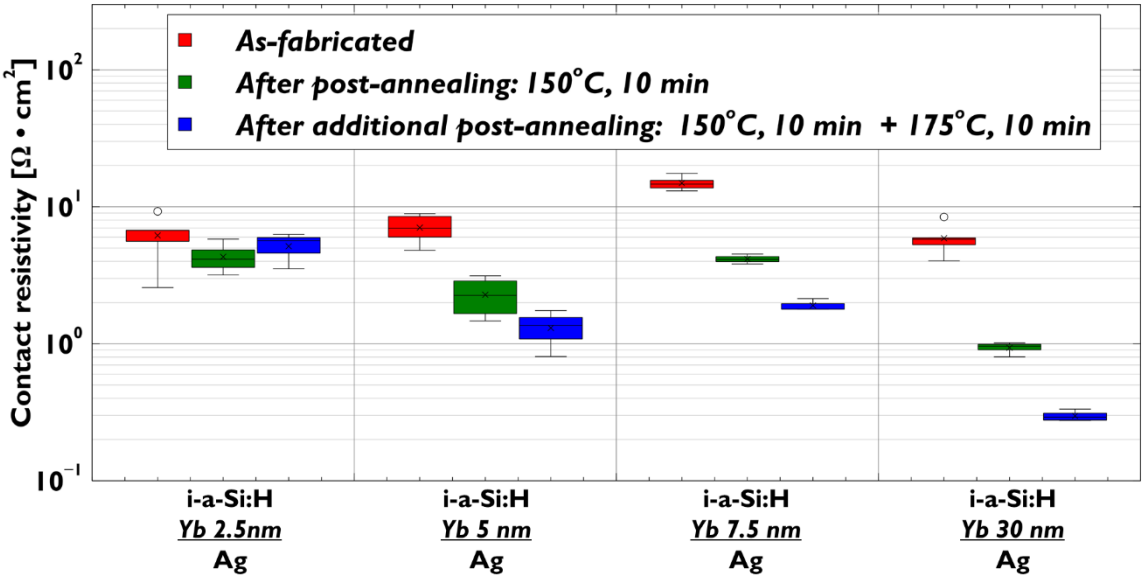

Figure 7. Evaluation of dependence of ρ_c on Yb thicknesses and annealing treatment before and after Yb/Ag deposition. Each box plot includes five data points.

Figure 7 plots the ρ_c for different Yb thicknesses and successive post-annealing treatments. Note that the ρ_c values in Figure 7 are relatively higher than those plotted in Figure 6. This difference is because of the difference in the initial a-Si:H thickness of about ~3 nm between the two sample sets. As mentioned in Section 3.1, for the samples shown in Figure 4 and Figure 6, an additional HF clean was used to etch the native SiO_x that was grown due to long storage time of more than a month. However,

for the samples shown in Figure 7, Yb deposition was immediately done after i-a-Si:H deposition of 7-8 nm and so a HF clean was not necessary. During solar cell fabrication, the targeted i-a-Si:H thickness before silicidation would be 5-6 nm because 7-8 nm thick a-Si:H was slightly etched by a HF clean before MoO_x deposition (Figure 3 (a)). Therefore, relatively low ρ_c below 0.1 $\Omega \cdot cm^2$ (similar to Figure 6) may be expected.

Despite the higher ρ_c values, two important observations can be elicited from the trends of Figure 7: 1) the minimum thickness of Yb that is required to achieve a decreasing trend in ρ_c upon annealing is 5 nm, and 2) thicker Yb exhibits higher reduction rate in ρ_c during consecutive post-annealing treatments at 150 °C and 175 °C for 10 min each. Thus, Yb thickness of at least 5 nm is probably required to form $YbSi_x$ which competes with the formation of Yb/Ag alloy (see Figure 4 (c)). Moreover, the lower ρ_c obatined when using thicker Yb layers and larger thermal budgets is possibly due to formation of a thicker $YbSi_x$ layer, and consequently thinner i-a-Si:H, in these cases.

While Yb with a thickness of 30 nm led to the lowest ρ_c, such a thickness may be too large and may completely consume the i-a-Si:H layer during the silicidation process and subsequent thermal treatments, leading to loss of passivation.

3.4. Comparison of MolYSili cells with reference classical SHJ electron contact cells

From the results of Section 3.2 and 3.3, Yb of 5 nm thickness appears to be optimal. However, Yb of 7.5 nm was chosen for MolYSili cell fabrication considering the deposition uniformity of the thin metal layer over a large Si substrate area of 6-inch. MolYSili cells were fabricated following the process flow given in Figure 3 (a) and with the structure as shown in Figure 3 (c), whereby the $YbSi_x$ is simultaneously formed during the contact sintering process, which is added process simplification that can be introduced. Another possibility for process simplification is the formation of $YbSi_x$ during module lamination (see Section 3.5). Reference cells having classical SHJ electron contacts (i/n-a-Si:H) were also prepared (see Figure 3 (a) and (b)).

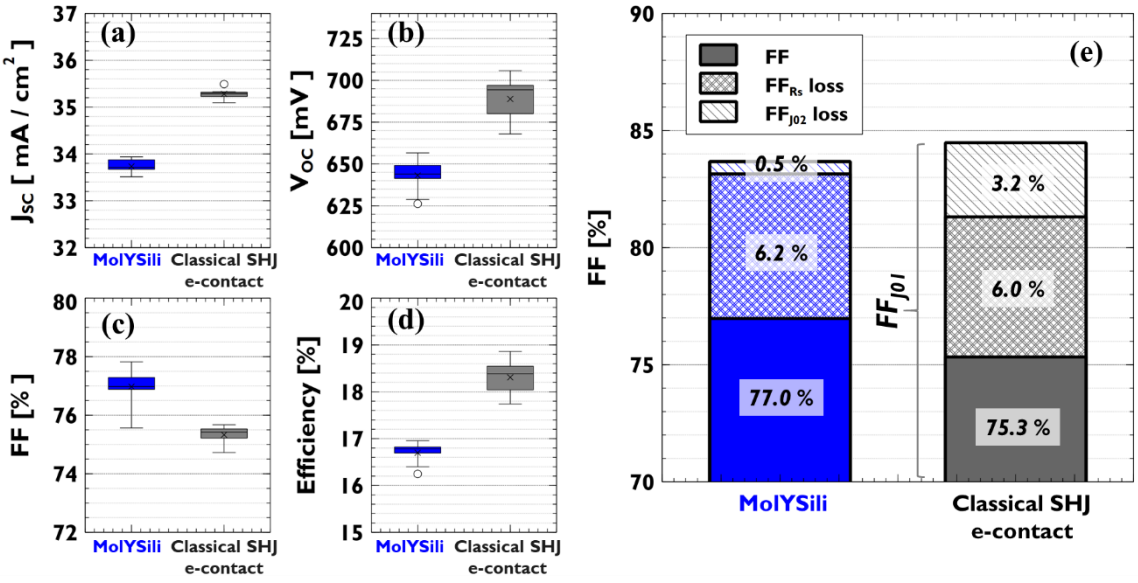

Figure 8. Illuminated IV parameter comparison between cells with 2 different electron contacts: $YbSi_x$ contact and reference i/n-a-Si:H contact. (a) J_{SC}, (b)V_{OC} (c) FF (d) efficiency. (e) FF loss analysis using average IV parameters based on Khanna method [61].

The first functional cells based on a-Si:H/$YbSi_x$-based electron contact with promising cell parameters were obtained as shown in Figure 8 and Table 1, albeit much lower in overall performance compared to the reference cells. The champion MolYSili cell exhibited a J_{SC} of 33.7 mA/cm^2, a V_{OC} of 654 mV, a *FF* of 76.9 %, and an efficiency of 17.0 %. In particular, the J_{SC} and the V_{OC} of MolYSili cells were found to be significantly lower than the reference cells. According to external quantum efficiency (EQE) results (not shown here), classical SHJ electron contact provides better optical rear reflectance, owing to the presence of the ITO optical buffer at the rear side, leading to higher J_{SC}. ITO also acts as a buffer between metal and the c-Si surface in the classical SHJ electron contact, which prevents excitation of surface plasmon polaritons, while in the a-Si:H/$YbSi_x$-contacted cells such a buffer is not present, which would lead to parasitic absorption losses in the near-infrared spectrum. The classical SHJ electron contact also offers higher passivation quality at the rear leading to better V_{OC} [37,38]. As shown in Figure 5, further optimization in Yb thickness in combination with annealing condition will increase the V_{OC} of MolYSili cells by achieving low $J_{0,metal}$.

The most significant aspect of the MolYSili cell performance is the higher FF attained with respect to our classical SHJ electron contact cells, even though both cell types exhibited similar series resistance, R_S (Table 1), which was extracted using Bowden method[62]. To investigate this in detail, a FF loss

analysis was done based on Khanna method [61], and the results are given in Figure 8 (e). The FF loss related to the shunt resistance is not mentioned due to its negligible contribution.

The main reason for the higher FF of the MolYSili cells was the lower *FF* loss due to J_{02}-like recombination (carrier recombination in the space charge region), FF_{J02}, of 0.5 % in such cells compared to 3.2 % in classical SHJ electron contact cells. This difference may be attributed to the absence of ITO sputtering damage on the rear side of MolYSili cells as compared to SHJ electron contact cells, which preserves the quality of the passivating i-a-Si:H layer.

Table 1. Average illuminated IV parameters by pre-annealing treatment and different electron contact structures.

Cell information	J_{SC} [mA/cm^2]	V_{OC} [mV]	FF [%]	Efficiency [%]	R_S [Ω·cm^2]
MolYSili	33.7 ± 0.2	643 ± 11	77.0 ± 0.7	16.7 ± 0.2	1.3 ± 0.2
Classical e$^-$ contact	35.3 ± 0.1	689 ± 15	75.3 ± 0.3	18.3 ± 0.4	1.4 ± 0.1

3.5. Damp heat testing of laminated MolYSili cells

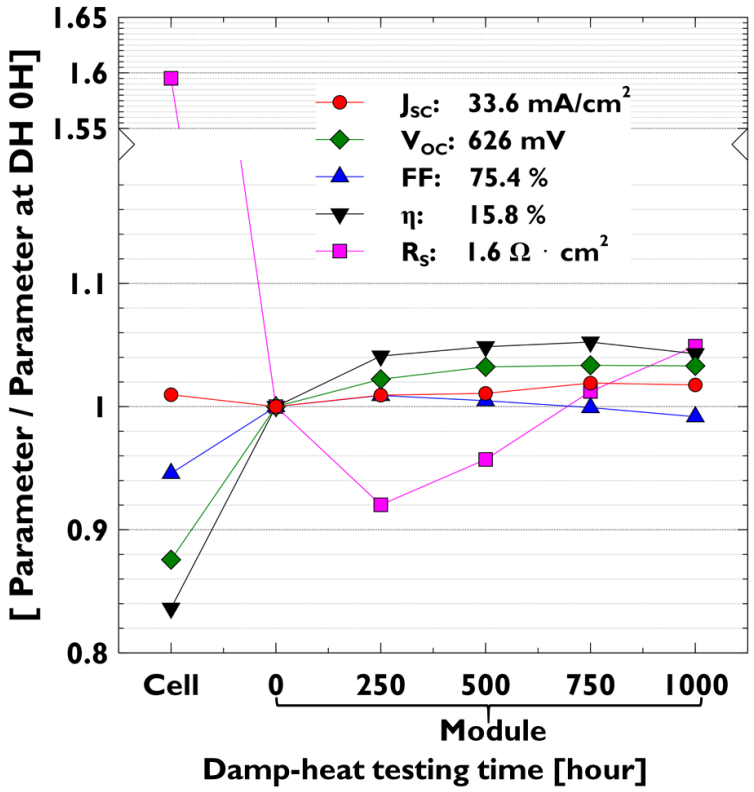

Figure 9. Damp-heat test results of the MolYSili cell in one-cell-mini-module. Normalized illuminated IV parameters by different testing time. The values mentioned in the legend are the measured one just after module lamination (DH 0h).

A mini-module was made using an Yb-contacted cell with a pre-annealing treatment at 300 ˚C and with an initial Yb thickness of 7.5 nm (shown in Figure 3 (a) and (d)). Note that the electron contact applied here at cell level is i-a-Si:H/Yb/Ag because Yb/Ag was evaporated after the contact sintering process. Therefore, in this case, $YbSi_x$ formation was combined with module lamination (150 °C, 20 min), which is another process simplification possibility. The thermal stability of the thus-formed MolYSili cell laminate was monitored by subjecting the mini-module to damp-heat testing under the standard conditions (85 °C, 85 % humidity, 1000 hour), and the results are plotted in Figure 9.

To understand the progress in IV parameters easily, all values were normalized using the value measured just after module fabrication. After module lamination, the illuminated IV parameters were significantly improved, which is expected to be due to the formation of $YbSi_x$. At the end of 1000 h, J_{SC}, V_{OC} and efficiency showed improvement while FF decreased slightly with an associated increase in R_S. Considering the criteria (degradation <5 $\%_{rel}$ in an efficiency) for the damp-heat test, the MolYSili mini-module was found to be very stable during the whole testing period.

4. Conclusions and outlook

Metal silicides, well-known as good contact layers, are also attractive candidates for use in doping-free silicon solar cells as part of passivating contacts based on a-Si:H, given their simple formation method. $YbSi_x$, in particular, would be a good candidate as an electron contact thanks to the low work function and low $E_{F,metal\text{-}silicide}$ pinning factor. $YbSi_x$ can be formed by reacting a-Si:H and Yb using a low temperature anneal below 200 °C, compatible with a-Si:H-based heterojunction cell technology. A low $J_{0,metal}$ of 5 fA/cm^2 was attained for the $YbSi_x$ contact formed by subjecting a 5nm thick Yb layer on an 8 nm thick a-Si:H layer to a 150 °C/10 min silicidation process. Substantial ρ_c reduction of ~10 times was also achieved after annealing Yb contacts under the same conditions (150 °C/10 min), due to the conversion of the i-a-Si:H/Yb contact to a a-Si:H/$YbSi_x$ contact and the consequent increase in the metal Fermi level pinning factor. The i-a-Si:H/$YbSi_x$ electron contact was integrated into doping-free Si solar cells with MoO_x based hole contact, called MolYSili cells. The champion MolYSili cell achieved a promising efficiency of 17.0 %, with a significantly better FF compared to cells with an i/n-a-Si:H reference electron contact, albeit with inferior V_{OC} and J_{SC}. After standard damp-heat testing for 1000

hours, no degradation was observed in the MolYSili mini-module efficiency. Considering GW-scale production of c-Si solar cells, Yb material may not be viable due to its low abundance in nature. However, more abundant low work function metals, such as Ca (Φ 2.9 eV), Sr (Φ 2.6 eV) and Ba (Φ 2.7 eV), can be used as alternatives. This work is proof-of-concept demonstration and feasibility of using the more abundant silicides for this application need to be explored in the future.

Acknowledgments

The authors thank Pieter Lagrain, Olivier Richard and Hugo Bender for TEM measurement. Moreover, the authors gratefully acknowledge the financial support of imec's industrial affiliation program for Si-PV. The work in this paper was partially funded by the Kuwait Foundation for the Advancement of Sciences under project number CN18-15EE-01. imec is a partner in EnergyVille (www.energyville.be), a collaboration between the Flemish research partners KU Leuven, VITO, imec, and UHasselt in the field of sustainable energy and intelligent energy systems.

References

(1) Werner, S.; Lohmüller, E.; Belledin, U.; Vlooswijk, A. H. G.; Naber, R. C. G.; Mack, S.; Wolf, A. Optimization of BBr3 Diffusion Processes for N-Type Silicon Solar Cells. In *31st European PV Solar Energy Conference and Exhibition*; 2015; Vol. 1, pp 14–18. https://doi.org/10.4229/EUPVSEC20152015-2AV.2.5.

(2) Wehmeier, N.; Nowack, A.; Lim, B.; Brendem??hl, T.; Kajari-Schr??der, S.; Schmidt, J.; Brendel, R.; Dullweber, T. 21.0%-Efficient Screen-Printed n-PERT Back-Junction Silicon Solar Cell with Plasma-Deposited Boron Diffusion Source. *Sol. Energy Mater. Sol. Cells* **2016**, *158*, 50–54. https://doi.org/10.1016/j.solmat.2016.05.054.

(3) Cho, J.; Shin, H.-N.-R.; Lee, J.; Choi, Y.; Lee, J.; Oh, H.; Kim, T.; Hwang, M.; Cho, E.-C. 21%-Efficient n-Type Rear-Junction PERT Solar Cell with Industrial Thin 156mm Cz Single Crystalline Silicon Wafer. *Energy Procedia* **2015**, *77*, 279–285. https://doi.org/10.1016/j.egypro.2015.07.039.

(4) John, J.; Hajjiah, A.; Haslinger, M.; Soha, M.; Urueña, A.; Cornagliotti, E.; Tous, L.; Mertens, P.; Poortmans, J. Deposition Behaviour of Metal Impurities in Acidic Cleaning Solutions and Their Impact on Effective Minority Carrier Lifetime in N-Type Silicon Solar Cells. *Sol. Energy Mater. Sol. Cells* **2019**, *194* (August 2018), 83–88. https://doi.org/10.1016/j.solmat.2019.02.001.

(5) Reiter, S.; Koper, N.; Reineke-Koch, R.; Larionova, Y.; Turcu, M.; Krügener, J.; Tetzlaff, D.; Wietler, T.; Höhne, U.; Kähler, J.-D.; Brendel, R., Peibst, R. Parasitic Absorption in Polycrystalline Si-Layers for Carrier-Selective Front Junctions. *Energy Procedia* **2016**, *92*, 199–204. https://doi.org/http://dx.doi.org/10.1016/j.egypro.2016.07.057.

(6) Cuevas, A.; Basore, P. A.; Giroult‐Matlakowski, G.; Dubois, C. Surface Recombination Velocity of Highly Doped n‐type Silicon. *J. Appl. Phys.* **1996**, *80* (6), 3370–3375. https://doi.org/10.1063/1.363250.

(7) Wan, Y.; Bullock, J.; Hettick, M.; Xu, Z.; Samundsett, C.; Yan, D.; Peng, J.; Ye, J.; Javey, A.; Cuevas, A. Temperature and Humidity Stable Alkali / Alkaline-Earth Metal Carbonates as Electron Heterocontacts for Silicon Photovoltaics. **2018**, *1800743*, 1–6. https://doi.org/10.1002/aenm.201800743.

(8) Bullock, J.; Hettick, M.; Geissbühler, J.; Ong, A. J.; Allen, T.; Sutter-Fella, C. M.; Chen, T.; Ota, H.; Schaler, E. W.; De Wolf, S.; Ballif, C., Cuevas, A., Javey A. Efficient Silicon Solar Cells with Dopant-Free Asymmetric Heterocontacts. *Nat. Energy* **2016**, *1* (3), 15031. https://doi.org/10.1038/nenergy.2015.31.

(9) Yu, J.; Fu, Y.; Zhu, L.; Yang, Z.; Yang, X.; Ding, L.; Zeng, Y.; Yan, B.; Tang, J.; Gao, P.; Ye, J. Heterojunction Solar Cells with Asymmetrically Carrier-Selective Contact Structure of Molybdenum-Oxide/Silicon/Magnesium-Oxide. *Sol. Energy* **2018**, *159*, 704–709. https://doi.org/10.1016/j.solener.2017.11.047.

(10) Wu, W.; Lin, W.; Zhong, S.; Paviet-Salomon, B.; Despeisse, M.; Liang, Z.; Boccard, M.; Shen, H.; Ballif, C. 22% Efficient Dopant-Free Interdigitated Back Contact Silicon Solar Cells. *AIP Conf. Proc.* **2018**, *1999*, 1–7. https://doi.org/10.1063/1.5049288.

(11) Yang, Z.; Gao, P.; Sheng, J.; Tong, H.; Quan, C.; Yang, X.; Chee, K. W. A.; Yan, B.; Zeng, Y.; Ye, J. Principles of Dopant-Free Electron-Selective Contacts Based on Tunnel Oxide/Low Work-Function Metal Stacks and Their Applications in Heterojunction Solar Cells. *Nano Energy* **2018**, *46* (January), 133–140. https://doi.org/10.1016/j.nanoen.2018.01.043.

(12) Wang, F.; Zhao, S.; Liu, B.; Li, Y.; Ren, Q.; Du, R.; Wang, N.; Wei, C.; Chen, X.; Wang, G.; Yan, B., Zhao, Y., Zhang, X. Silicon Solar Cells with Bifacial Metal Oxides Carrier Selective Layers. *Nano Energy* **2017**, *39* (June), 437–443. https://doi.org/10.1016/j.nanoen.2017.07.014.

(13) Um, H. D.; Kim, N.; Lee, K.; Hwang, I.; Seo, J. H.; Seo, K. Dopant-Free All-Back-Contact Si Nanohole Solar Cells Using MoOx and LiF Films. *Nano Lett.* **2016**, *16* (2), 981–987. https://doi.org/10.1021/acs.nanolett.5b03955.

(14) Tong, H.; Yang, Z.; Wang, X.; Liu, Z.; Chen, Z.; Ke, X.; Sui, M.; Tang, J.; Yu, T.; Ge, Z.; Zeng, Y., Gao, P., Ye, J. Dual Functional Electron-Selective Contacts Based on Silicon Oxide/Magnesium: Tailoring Heterointerface Band Structures While Maintaining Surface Passivation. *Adv. Energy Mater.* **2018**, *8* (16), 1702921.

https://doi.org/10.1002/aenm.201702921.
(15) Wu, W.; Bao, J.; Jia, X.; Liu, Z.; Cai, L.; Liu, B.; Song, J. Dopant-Free Back Contact Silicon Heterojunction Solar Cells Employing Transition Metal Oxide Emitters. *Phys. status solidi - Rapid Res. Lett.* **2016**, *6* (August 2016), 1–6. https://doi.org/10.1002/pssr.201600254.
(16) Wong, K. H.; Ananthanarayanan, K.; Luther, J.; Balaya, P. Origin of Hole Selectivity and the Role of Defects in Low-Temperature Solution-Processed Molybdenum Oxide Interfacial Layer for Organic Solar Cells. *J. Phys. Chem. C* **2012**, *116* (31), 16346–16351. https://doi.org/10.1021/jp303679y.
(17) Macco, B.; Vos, M. F. J.; Thissen, N. F. W.; Bol, A. A.; Kessels, W. M. M. Low-Temperature Atomic Layer Deposition of MoOx for Silicon Heterojunction Solar Cells. *Phys. status solidi - Rapid Res. Lett.* **2015**, *9* (7), 393–396. https://doi.org/10.1002/pssr.201510117.
(18) Neusel, L.; Bivour, M.; Hermle, M. Selectivity Issues of MoOx Based Hole Contacts. In *SiliconPV conference 2017*; 2017; Vol. 124, pp 425–434. https://doi.org/10.1016/j.egypro.2017.09.268.
(19) Bivour, M.; Zähringer, F.; Ndione, P.; Hermle, M. Sputter-Deposited WOx and MoOx for Hole Selective Contacts. In *SiliconPV conference 2017*; 2017; Vol. 124, pp 400–405. https://doi.org/10.1016/j.egypro.2017.09.259.
(20) Geissbühler, J.; Werner, J.; Martin De Nicolas, S.; Barraud, L.; Hessler-Wyser, A.; Despeisse, M.; Nicolay, S.; Tomasi, A.; Niesen, B.; De Wolf, S.; Ballif, C. 22.5% Efficient Silicon Heterojunction Solar Cell with Molybdenum Oxide Hole Collector. *Appl. Phys. Lett.* **2015**, *107* (8), 081601. https://doi.org/10.1063/1.4928747.
(21) Cho, J.; Nawal, N.; Hadipour, A.; Recaman Payo, M.; van der Heide, A.; Radhakrishnan, H. S.; Debucquoy, M.; Gordon, I.; Szlufcik, J.; Poortmans, J. Interface Analysis and Intrinsic Thermal Stability of MoOx Based Hole-Selective Contacts for Silicon Heterojunction Solar Cells. *Sol. Energy Mater. Sol. Cells* **2019**, *201*, 110074. https://doi.org/10.1016/j.solmat.2019.110074.
(22) Cho, J.; Sivaramakrishnan Radhakrishnan, H.; Sharma, R.; Recaman Payo, M.; Debucquoy, M.; van der Heide, A.; Gordon, I.; Szlufcik, J.; Poortmans, J. Thermal Stability Improvement of Metal Oxide-Based Contacts for Silicon Heterojunction Solar Cells. *Sol. Energy Mater. Sol. Cells* **2019**, *in press*, 110324. https://doi.org/10.1016/j.solmat.2019.110324.
(23) Yang, X.; Zheng, P.; Bi, Q.; Weber, K. Silicon Heterojunction Solar Cells with Electron Selective TiOx Contact. *Sol. Energy Mater. Sol. Cells* **2016**, *150*, 32–38. https://doi.org/10.1016/j.solmat.2016.01.020.
(24) Yang, X.; Bi, Q.; Ali, H.; Davis, K.; Schoenfeld, W. V; Weber, K. High-Performance TiO2-Based Electron-Selective Contacts for Crystalline Silicon Solar Cells. *Adv. Mater.* **2016**, *28* (28), 5891–5897. https://doi.org/10.1002/adma.201600926.
(25) Wan, Y.; Samundsett, C.; Bullock, J.; Hettick, M.; Allen, T.; Yan, D.; Peng, J.; Wu, Y.; Cui, J.; Javey, A.; Cuevas, A. Conductive and Stable Magnesium Oxide Electron-Selective Contacts for Efficient Silicon Solar Cells. *Adv. Energy Mater.* **2017**, *7* (5), 1601863. https://doi.org/10.1002/aenm.201601863.
(26) Macco, B.; Bivour, M.; Deijkers, J. H.; Basuvalingam, S. B.; Black, L. E.; Melskens, J.; Van De Loo, B. W. H.; Berghuis, W. J. H.; Hermle, M.; Kessels, W. M. M. Effective Passivation of Silicon Surfaces by Ultrathin Atomic-Layer Deposited Niobium Oxide. *Appl. Phys. Lett.* **2018**, *112* (24), 1–5. https://doi.org/10.1063/1.5029346.
(27) Yang, X.; Aydin, E.; Xu, H.; Kang, J.; Hedhili, M.; Liu, W.; Wan, Y.; Peng, J.; Samundsett, C.; Cuevas, A.; De Wolf, S. Tantalum Nitride Electron-Selective Contact for Crystalline Silicon Solar Cells. *Adv. Energy Mater.* **2018**, *8* (20), 1800608. https://doi.org/10.1002/aenm.201800608.
(28) Yang, X.; Liu, W.; De Bastiani, M.; Allen, T.; Kang, J.; Xu, H.; Aydin, E.; Xu, L.; Bi, Q.; Dang, H.; AlHabshi, E., Kotsovos, K., AlSaggaf, A., Gereige, I., Wan, Y., Peng, J., Samundsett, C., Cuevas, A., De Wolf, S. Dual-Function Electron-Conductive, Hole-Blocking Titanium Nitride Contacts for Efficient Silicon Solar Cells. *Joule* **2019**, *3* (5), 1314–1327. https://doi.org/10.1016/j.joule.2019.03.008.
(29) Bullock, J.; Zheng, P.; Jeangros, Q.; Tosun, M.; Hettick, M.; Sutter-Fella, C. M.; Wan, Y.; Allen, T.; Yan, D.; Macdonald, D.; De Wolf, S., Hessler-Wyser, A., Cuevas, A., Javey A. Lithium Fluoride Based Electron Contacts for High Efficiency N-Type Crystalline Silicon Solar Cells. *Adv. Energy Mater.* **2016**, *6* (14). https://doi.org/10.1002/aenm.201600241.

(30) Wan, Y.; Samundsett, C.; Bullock, J.; Allen, T.; Hettick, M.; Yan, D.; Zheng, P.; Zhang, X.; Cui, J.; McKeon, J.; Javey A., Cuevas, A. Magnesium Fluoride Electron-Selective Contacts for Crystalline Silicon Solar Cells. *ACS Appl. Mater. Interfaces* **2016**, *8* (23), 14671–14677. https://doi.org/10.1021/acsami.6b03599.
(31) Allen, T. G.; Bullock, J.; Zheng, P.; Vaughan, B.; Barr, M.; Wan, Y.; Samundsett, C.; Walter, D.; Javey, A.; Cuevas, A. Calcium Contacts to N-Type Crystalline Silicon Solar Cells. *Prog. Photovoltaics Res. Appl.* **2017**, *25* (7), 636–644. https://doi.org/10.1002/pip.2838.
(32) Allen, T. G.; Bullock, J.; Jeangros, Q.; Samundsett, C.; Wan, Y.; Cui, J.; Hessler-Wyser, A.; De Wolf, S.; Javey, A.; Cuevas, A. A Low Resistance Calcium/Reduced Titania Passivated Contact for High Efficiency Crystalline Silicon Solar Cells. *Adv. Energy Mater.* **2017**, *7* (12), 1602606. https://doi.org/10.1002/aenm.201602606.
(33) Wan, Y.; Samundsett, C.; Yan, D.; Allen, T.; Peng, J.; Cui, J.; Zhang, X.; Bullock, J.; Cuevas, A. A Magnesium/Amorphous Silicon Passivating Contact for n -Type Crystalline Silicon Solar Cells. *Appl. Phys. Lett.* **2016**, *109* (11), 113901. https://doi.org/10.1063/1.4962960.
(34) Cho, J.; Debucquoy, M.; Recaman Payo, M.; Malik, S.; Filipič, M.; Radhakrishnan, H. S.; Bearda, T.; Gordon, I.; Szlufcik, J.; Poortmans, J. Contact Resistivity Reduction on Lowly-Doped n-Type Si Using a Low Work Function Metal and a Thin TiOx Interfacial Layer for Doping-Free Si Solar Cells. In *SiliconPV conference 2017*; 2017; Vol. 124, pp 842–850. https://doi.org/10.1016/j.egypro.2017.09.356.
(35) Cho, J.; Debucquoy, M.; Payo, M. R.; Schapmans, E.; Gordon, I.; Szlufcik, J.; Poortmans, J. Evidence of TiOx Reduction at the SiOx/TiOx Interface of Passivating Electron-Selective Contacts. In *SiliconPV conference 2018*; 2018; Vol. 040005, p 040005. https://doi.org/10.1063/1.5049268.
(36) Cho, J.; Payo, M. R.; Debucquoy, M.; Radhakrishnan, H. S.; Gordon, I.; Szlufcik, J.; Ghannam, M.; Poortmans, J. Electron-Selective Contact Using i-a-Si:H/TiOx/Yb/Ag Stack for Silicon Heterojunction Solar Cells. In *35th European Photovoltaic Solar Energy Conference and Exhibition*; 2018; pp 431–433. https://doi.org/10.4229/35thEUPVSEC20182018-2CO.11.5.
(37) Cho, J.; Melskens, J.; Payo, M. R.; Debucquoy, M.; Radhakrishnan, H. S.; Gordon, I.; Szlufcik, J.; Kessels, W. M. M. M.; Poortmans, J. Performance and Thermal Stability of an A-Si:H/TiO x /Yb Stack as an Electron-Selective Contact in Silicon Heterojunction Solar Cells. *ACS Appl. Energy Mater.* **2019**, *2* (2), 1393–1404. https://doi.org/10.1021/acsaem.8b01969.
(38) Cho, J.; Melskens, J.; Debucquoy, M.; Recamán Payo, M.; Jambaldinni, S.; Bearda, T.; Gordon, I.; Szlufcik, J.; Kessels, W. M. M.; Poortmans, J. Passivating Electron-Selective Contacts for Silicon Solar Cells Based on an a-Si:H/TiOx Stack and a Low Work Function Metal. *Prog. Photovoltaics Res. Appl.* **2018**, *26* (10), 835–845. https://doi.org/10.1002/pip.3023.
(39) Souza, J. P. de; Hovel, H. J.; Inns, D.; Kim, J.; Lavoie, C.; Eugene, C.; Sadana, D. K.; Saenger, K. L.; Shahidi, G.; Shahrijerdi, D.; Zhang, Z. Schottky Barrier Solar Cells with High and Low Work Function Metal Contacts. US 2012/0285517 A1, 2012.
(40) Borland, W.; Maria, J.-P. Compositions and Processes for Forming Photovoltaic Devices. WO 2010/019532 A2, 2010.
(41) Lee, W.-J.; Kim, D.-W.; Oh, S.-Y.; Kim, Y.-J.; Zhang, Y.-Y.; Zhong, Z.; Li, S.-G.; Jung, S.-Y.; Han, I.-S.; Gu, T.; Bae, T.-S., Lee, G.-W., Wang, J.-S., Lee, H.-D. Work Function Variation of Nickel Silicide Using an Ytterbium Buffer Layer for Schottky Barrier Metal-Oxide-Semiconductor Field-Effect Transistors. *J. Appl. Phys.* **2007**, *101* (10), 103710. https://doi.org/10.1063/1.2734882.
(42) Nemanich, R. J.; Fiordalice, R. W.; Jeon, H. Raman Scattering Characterization of Titanium Silicide Formation. *IEEE J. Quantum Electron.* **1989**, *25* (5), 997–1002. https://doi.org/10.1109/3.27991.
(43) Larson, J. M.; Snyder, J. P. Overview and Status of Metal S/D Schottky-Barrier MOSFET Technology. *IEEE Trans. Electron Devices* **2006**, *53* (5), 1048–1058. https://doi.org/10.1109/TED.2006.871842.
(44) Kuroda, R.; Tanaka, H.; Nakao, Y.; Teramoto, A.; Miyamoto, N.; Sugawa, S.; Ohmi, T. Ultra-Low Series Resistance W/ErSi2/N+-Si and W/Pd2Si/P+-Si S/D Electrodes for Advanced CMOS Platform. *Tech. Dig. - Int. Electron Devices Meet. IEDM* **2010**, 26.2.1-26.2.4.
(45) Zhu, S.; Chen, J.; Li, M. F.; Lee, S. J.; Singh, J.; Zhu, C. X.; Du, A.; Tung, C. H.; Chin, A.;

Kwong, D. L. N-Type Schottky Barrier Source/Drain MOSFET Using Ytterbium Silicide. *IEEE Electron Device Lett.* **2004**, *25* (8), 565–567. https://doi.org/10.1109/LED.2004.831582.
(46) Yarekha, D. A.; Larrieu, G.; Breil, N.; Dubois, E.; Godey, S.; Wallart, X.; Soyer, C.; Remiens, D.; Reckinger, N.; Tang, X.; Laszcz, A., Ratajczak, J., Halimaoui, A. UHV Fabrication of the Ytterbium Silicide as Potential Low Schottky Barrier S/D Contact Material for N-Type MOSFET. In *ECS Transactions*; ECS, 2009; Vol. 19, pp 339–344. https://doi.org/10.1149/1.3118961.
(47) Lin, L.; Guo, Y.; Robertson, J. Metal Silicide Schottky Barriers on Si and Ge Show Weaker Fermi Level Pinning. *Appl. Phys. Lett.* **2012**, *101* (5), 052110. https://doi.org/10.1063/1.4742861.
(48) Wronski, C. R.; Carlson, D. E. Surface States and Barrier Heights of Metal-Amorphous Silicon Schottky Barriers. *Solid State Commun.* **1977**, *23* (7), 421–424. https://doi.org/10.1016/0038-1098(77)90999-1.
(49) Bivour, M. *SILICON HETEROJUNCTION SOLAR CELLS: ANALYSIS AND BASIC UNDERSTANDING*; Fraunhofer Verlag, 2017.
(50) Chen, L. J. *Silicide Technology for Integrated Circuits*; Chen, L. J., Ed.; IET: The Institution of Engineering and Technology, Michael Faraday House, Six Hills Way, Stevenage SG1 2AY, UK, 2004. https://doi.org/10.1049/PBEP005E.
(51) Kawazu, Y.; Kudo, H.; Onari, S.; Arai, T. Low-Temperature Crystallization of Hydrogenated Amorphous Silicon Induced by Nickel Silicide Formation. *Jpn. J. Appl. Phys.* **1990**, *29* (Part 1, No. 12), 2698–2704. https://doi.org/10.1143/JJAP.29.2698.
(52) Na, S.; Choi, H.; Lee, B.; Choi, J.; Seo, Y.; Kim, H.; Lee, S. H.; Lee, H. J. A Study on the Formation Mechanism of Ytterbium Silicide for Schottky Contact Applications. *Surf. Interface Anal.* **2012**, *44* (11–12), 1497–1502. https://doi.org/10.1002/sia.4985.
(53) Lee, R. T. P.; Lim, A. E. J.; Tan, K. M.; Liow, T. Y.; Lo, G. Q.; Samudra, G. S.; Chi, D. Z.; Yeo, Y. C. N-Channel FinFETs with 25-Nm Gate Length and Schottky-Barrier Source and Drain Featuring Ytterbium Silicide. *IEEE Electron Device Lett.* **2007**, *28* (2), 164–167. https://doi.org/10.1109/LED.2006.889233.
(54) Schroder, D. K. *Semiconductor Material and Device Characterization, Third Edition*; John Wiley & Sons, Inc.: Hoboken, NJ, USA, 2005; Vol. 44. https://doi.org/10.1002/0471749095.
(55) Haslinger, M.; Soha, M.; Jambaldinni, S.; Hajjiah, A.; Szlufcik, J.; Poortmans, J.; John, J. Novel Wet Chemical Cleaning Concepts for High Efficiency Silicon Solar Cells. In *33rd European Photovoltaic Solar Energy Conference and Exhibition*; 2017; pp 628–630.
(56) Yoon, S. Y.; Oh, J. Y.; Kim, C. O.; Jang, J. Low Temperature Solid Phase Crystallization of Amorphous Silicon Using (Au + Ni) Solution. *Solid State Commun.* **1998**, *106* (6), 325–328. https://doi.org/10.1016/S0038-1098(98)00064-7.
(57) Jang, J.; Oh, J. Y.; Kim, S. K.; Choi, Y. J.; Yoon, S. Y.; Kim, C. O. Electric-Field-Enhanced Crystallization of Amorphous Silicon. *Nature* **1998**, *395* (6701), 481–483. https://doi.org/10.1038/26711.
(58) Green, M. A.; Blakers, A. W.; Zhao, J.; Milne, A. M.; Wang, A.; Dai, X. Characterization of 23-Percent Efficient Silicon Solar Cells. *IEEE Trans. Electron Devices* **1990**, *37* (2), 331–336. https://doi.org/10.1109/16.46361.
(59) Glunz, S. W.; Nekarda, J.; Mäckel, H.; Cuevas, A. Analyzing Back Contacts of Silicon Solar Cells by Suns-Voc-Measurements at High Illumination Densities. In *Proceedings of the 22nd European Photovoltaic Solar Energy Conference, 3-7 September 2007, Milan, Italy*; 2007; pp 849–853.
(60) Yu, H.; Schaekers, M.; Schram, T.; Demuynck, S.; Horiguchi, N.; Barla, K.; Collaert, N.; Thean, A. V.-Y.; De Meyer, K. Thermal Stability Concern of Metal-Insulator-Semiconductor Contact: A Case Study of Ti/TiO 2 /n-Si Contact. *IEEE Trans. Electron Devices* **2016**, *63* (7), 2671–2676. https://doi.org/10.1109/TED.2016.2565565.
(61) Khanna, A.; Mueller, T.; Stangl, R. A.; Hoex, B.; Basu, P. K.; Aberle, A. G. A Fill Factor Loss Analysis Method for Silicon Wafer Solar Cells. *IEEE J. Photovoltaics* **2013**, *3* (4), 1170–1177. https://doi.org/10.1109/JPHOTOV.2013.2270348.
(62) Bowden, S.; Rohatgi, A. Rapid and Accurate Determination of Series Resistance and Fill Factor Losses in Industrial Silicon Solar Cells. In *17th European Photovoltaic Solar Energy Conference and Exhibition*; Munich, Germany, 2001.

Table of Contents Graphic